Check for updates

Sea urchin-like Bi₂S₃/curcumin heterojunction rapidly kills bacteria and promotes wound healing under near-infrared light†

Danya Wan,[a] Xiangmei Liu,*[a,b] Wenchan Sun,[a] Yuqian Qiao,[c] Da-fu Chen,*[d] Yufeng Zheng [ID][c] and Shuilin Wu [ID] *[c]

Bacterial infection is an urgent public health problem. We design a novel photo-responsive hybrid material by growing small molecules of curcumin (Cur) *in situ* on a sea urchin-like Bi₂S₃ surface by a one-step hydrothermal reaction method, thus forming an organic–inorganic hybrid material with interfacial contact. The Bi₂S₃/Cur hybrid material has good antibacterial effect under 808 nm near-infrared (NIR) light irradiation. The antibacterial mechanism is that the electron redistribution at the interface of Bi₂S₃/ Cur excited by 808 nm NIR light will cause a large number of electrons to gather on the side of Bi₂S₃, forming an internal electric field to drive the excited electrons from Bi₂S₃ to Cur, which accelerates the separation of photoexcited electron–hole pairs and enhances the production of reactive oxygen species (ROS). In conclusion, due to these synergistic effects of the photothermal properties of Bi₂S₃, the production of more ROS and the release of small molecules of Cur from traditional Chinese medicine in Bi₂S₃/Cur, the antibacterial efficacy against *Staphylococcus aureus* (*S. aureus*) and *Escherichia coli* (*E. coli*) is 99.96% and 99.03%, respectively. *In vivo* experiments in animals show that Bi₂S₃/Cur can reduce the inflammatory response and promote wound healing. This paper presents a simple, rapid and safe strategy for the treatment of wound infections with near-infrared light.

1. Introduction

Bacterial infection is a serious problem for wounds during the healing process. Because bacteria multiply rapidly, they can easily cause persistent wound infections and have the potential to spread to others and cause other diseases.[1,2] Antibiotics are specific anti-microbial drugs, and long-term or repeated use of antibiotics can easily cause bacterial resistance and negatively affect patient health through side effects. Some reports estimate that by 2050, 10 million people will die each year from bacterial infections. This has led to concerns about a "post-antibiotic era" in which many bacterial infections cannot be treated.[2–5] Therefore, it is of great significance to explore and develop a treatment method that can effectively sterilize bacteria without drug resistance.

In recent years, photoresponsive biomedical materials have provided a possibility for efficient sterilization. Some inorganic semiconductors with photoresponsive properties have been extensively studied, such as CuS,[6,7] MoS₂,[8,9] Bi₂S₃,[10] AuNRs[11] *etc*. These photoresponsive materials can effectively separate electrons and holes under light stimulation, thus accelerating the photocatalytic reaction.[12–14] Photocatalytic sterilization includes photodynamic anti-bacterial (PDA) and photothermal anti-bacterial (PTA).[15–18] PDA antibacterial produces reactive oxygen species (ROS), including ¹O₂, ·OH and ·O²⁻, which can kill bacteria by damaging cell membranes and/or DNA.[19,20] PTA causes bacterial cell membrane rupture and cell contents denatuation and inactivation by raising ambient temperature, leading to bacterial death.[21,22] Bi₂S₃ as a highly photoconductive semiconductor, has a narrow band gap (1.3–1.7 eV).[23] This material plays an important role in different research fields, such as photoconductive material, lithium ion battery, electrochemical hydrogen evolution and X-ray imaging, *etc*.[24–27] The photothermal effect generated by its excellent biocompatibility and intrinsic band gap absorption can be used as an antibacterial material in the photocatalytic antibacterial process.[28] Bi₂S₃ can generate electrons and holes under near-infrared

[a]Ministry-of-Education Key Laboratory for the Green Preparation and Application of Functional Materials, Hubei Key Laboratory of Polymer Materials, School of Materials Science & Engineering, Hubei University, Wuhan 430062, China. E-mail: liuxiangmei1978@163.com

[b]School of Health Science and Biomedical Engineering, Hebei University of Technology, Tianjin 300401, China

[c]School of Materials Science & Engineering, Peking University, Yiheyuan Road 5#, Beijing 100871, China. E-mail: slwu@pku.edu.cn

[d]Beijing JiShuiTan Hospital, Beijing Research Institute Orthopaedics & Traumatology, Lab Bone Tissue Engineering, Beijing 100035, Peoples R China. E-mail: chendfjst@126.com

†Electronic supplementary information (ESI) available. See DOI: https://doi.org/10.1039/d2bm01474b

light, and react with surrounding water or oxygen to produce ROS, but the separated electron holes will recombine quickly, so they are rarely used in photocatalytic reactions alone.[23]

With the first proposal of Chinese medicine material science, Chinese medicine small molecule materials have attracted more and more attention. The previous studies have reported tea nanoclusters as β-lactamase inhibitors for the treatment of multidrug-resistant bacterial pneumonia,[29] as well as the use of tea nanodots containing eight tea catechins with an average size of about 3 nm to kill MRSA and treat MRSA-H1N1 pneumonia.[30] In addition, Garcinia nanoparticles can effectively kill Gram-negative bacteria under microwave-assisted action,[31] and there is also MoS_2/FeS polarization with Rhein interface to enhance microwave-catalyzed treatment of bacterial infections of osteomyelitis.[32] Similarly, under the synergistic excitation of near-infrared light and ultrasound, CuS forms a tight interface with curcumin to achieve rapid broad-spectrum bactericidal action.[6] Curcumin is a natural herbal small molecule,[33] easy to chelate metal ions can reduce Cur insoluble in water and easy to remove and other shortcomings,[34] has a broad application prospect in the field of antibacterial biological materials.

In this paper, we constructed a Bi_2S_3/Cur hybrid material rapid sterilization system through interface contact. Cur is an organic semiconductor, and in the hydrothermal process, curcumin nanoparticles grow *in situ* on bismuth sulfide nanorods to form the contact interface of organic–inorganic mixed materials. Under the excitation of near-infrared light at 808 nm, the electron transfer from Bi_2S_3 to Cur is accelerated, and the photoelectron–hole pair of bismuth sulfide is effectively separated, which improves the photocatalytic efficiency of Bi_2S_3 and increases the generation of ROS. Therefore, Bi_2S_3/Cur can effectively kill *Staphylococcus aureus* (*S. aureus*) and *Escherichia coli* (*E. coli*) with the synergistic effect of PDT, PTT and Cur's bactericidal properties, with antibacterial rates up to 99.96% and 99.03%, respectively. The bactericidal mechanism of Bi_2S_3/Cur is shown in Scheme 1.
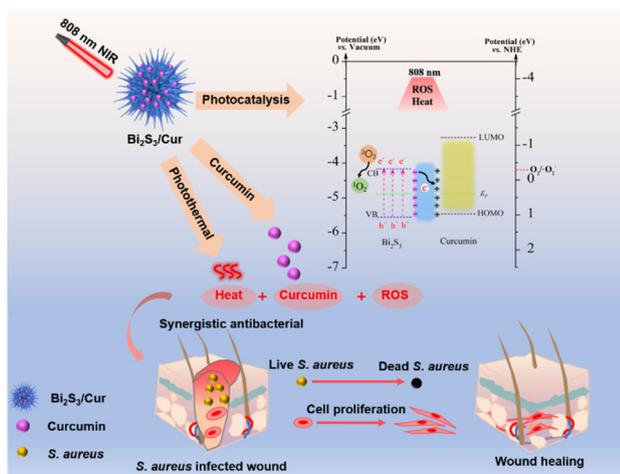
Scheme 1 Schematic diagram of Bi_2S_3/Cur photocatalysis and photothermal synergistic bactericidal effect under 808 nm near infrared light.

2. Experimental procedural

2.1. Synthetic sea urchin-shaped Bi_2S_3/Cur and Bi_2S_3 microspheres

The synthesis method of Bi_2S_3/Cur is based on previous work.[35] 1.46 g $Bi(NO_3)_3 \cdot 5H_2O$ and 0.2 g Curcumin (Cur) were weighed in a beaker, 40 mL Ethylene glycol was added into the beaker, and solution A was obtained after magnetic stirring for 1 h. In addition, Put the appropriate amount of thioureas (CS(NH$_2$)$_2$) was dissolved in 30 mL glycol for magnetic stirring for 1 h, and solution B was obtained. Solution B was slowly added to solution A and stirred for 30 min, then transferred to a Teflon-lined stainless steel autoclave with a volume of 100 mL, heated at 150 °C for 2 h and cooled to room temperature. Deionized water of equal volume was mixed and placed for a period of time, centrifuged at 10 000 rpm for 10 min, and washed with deionized water and ethanol for three times to obtain solid products. Bi_2S_3/Cur microspheres were dried and ground in an oven at 60 °C. Bi_2S_3 was obtained by the same preparation process except the addition of Cur. The synthesis process is illustrated as Scheme 2.

2.2. Characterization

Transmission electron microscope (TEM, Tecnai G20, FEI, USA) was used to observe the microstructure of the material, and field emission scanning electron microscope (FE-SEM JSM7100F, JEOL, JP) was used to observe the morphology of the material. The material composition and phase structure were determined by X-ray diffraction (XRD, D8A25, Bruker, Germany). The chemical structure of the samples was analyzed by Fourier Transform infrared spectroscopy (FTIR) (Nicolet 570). The elemental composition of the material was determined by X-ray photoelectron spectroscopy (XPS, ESCALAB 250Xi, Thermo Scientific, USA). The UV-Vis diffuse reflectance (DRS) spectra of the samples were measured by UV-Vis spectrophotometer (UV-3600, Shimadu, JP) with a wavelength between 200 and 900 nm. The material photocurrent density and electrochemical impedance spectroscopy (EIS) were measured by an electrochemical workstation (CHI660E, China). The photothermal curves and images were measured on FLIR (E50, Estonia). Electron spin resonance (ESR) was measured on the JESS – FA200 spectrometer (JEOL, JP). A light source (808 nm, LOS-BLD-0808) was utilized to produce the photothermal and photodynamic effects.

Scheme 2 Schematic diagram of Bi_2S_3/Cur hybrid material synthesis.

2.3. Loading of Cur

All of the measurements were tested by the microplate reader (SpectraMxi3, Molecular Devices). To determine the loading, we first measured the position of the maximum absorption peak of Cur at a known concentration of 10 µg mL^{-1} in ethanol solution, and the experimental results showed that there was a clear absorption peak of Cur at 430 nm. Then the absorbance of the concentrations of 0.625, 1.25, 2.5, 5, 10, 20, 40 µg mL^{-1} was measured at 430 nm to establish the Cur standard curve. The eqn (1) of the standard curve:

$$y = 0.03805\ x + 0.04146 \tag{1}$$

where y is the relative intensity and x is the sample concentration. To determine the loading of Cur in 0.5 mg mL^{-1} samples, all samples were continuously sonicated for 4 h to completely dissolve Cur in ethanol, and the supernatant was diluted 100 times and 100 µL was taken to determine the absorbance at 430 nm in a microplate reader.

2.4. Photothermal and photothermal conversion efficiency

The material with a concentration of 0.5 mg mL^{-1} (Cur, Bi$_2$S$_3$, Bi$_2$S$_3$/Cur) was placed in a 2 mL EP tube and irradiated by 808 nm NIR and 0.67 W cm^{-2} at the time of 200 s. Thermal imager records solution temperature and image. After 200 s irradiation, the temperature of the cooling section was recorded every 20 s until it was close to room temperature, and the photothermal conversion efficiency was calculated by three cycles. The material was irradiated with an initial light source power of 0.67 W cm^{-2} at the time of 200 s and then reduced to 0.24 W cm^{-2} for 20 min. Under the condition of spot diameter of 1.4 cm, the heating curve of the sample at 808 nm NIR was measured and the photothermal conversion efficiency was calculated.

The photothermal conversion efficiency (η) of Bi$_2$S$_3$/Cur can be obtained by the following eqn (2):

$$\eta = \frac{hST_{max} - T_0 - Q}{I(1 - 10^{-A})} \tag{2}$$

where, H is the heat transfer coefficient, S is the surface area of the container, T_{max} is the highest equilibrium temperature in the heating process, T_0 is the ambient temperature, Q is the heat absorption rate of 1.5 mL centrifugal tube (polystyrene), I is power of 808 nm NIR, A is the absorbance of Bi$_2$S$_3$/Cur at 808 nm.

In the cooling process, the time constant (τ_s) of Bi$_2$S$_3$/Cur is calculated by the following eqn (3):

$$t = -\tau_S \ln \theta = -\tau_S \ln \frac{T - T_0}{T_{max} - T_0}. \tag{3}$$

Assuming that the heat absorption and heat output of the system are equal, then substitute the eqn (4):

$$hS \approx \frac{m_{H_2O}C_{H_2O}}{\tau_S} \tag{4}$$

m_{H_2O} and C_{H_2O} are the mass and specific heat capacities of water respectively.

2.5. Photoelectrochemical measurements

The photoelectrochemical properties of Cur, Bi$_2$S$_3$ and Bi$_2$S$_3$/Cur were determined by Electrochemical workstation. The electrolyte was 0.5 mol L^{-1} Na$_2$SO$_4$ aqueous solution, and 3 mg mL^{-1} sample solution was prepared with deionized water. 100 µL mixed solution was dropped onto fluoride–tin oxide conductor glass with a pipette gun, and dried in air to form a uniform film for testing.

2.6. Detection of reactive oxygen species (ROS)

ROS production was detected using 2,7-dichlorodihydrofluorescein diacetate (DCFH-DA) assay kit, and ROS production was determined using DCFH probe. All tests were conducted in the dark to eliminate the effects of light. All samples (Cur, Bi$_2$S$_3$ and Bi$_2$S$_3$/Cur) were placed in 96-well plates, and 100 µL DCFH and 100 µL 1 mg mL^{-1} material were added to each well. Each sample was irradiated with 808 nm NIR (power density: 0.67 W cm^{-2}) for 20 min, and measured every 4 min with a microplate reader (wavelength: 488 nm and 525 nm). For the detection of singlet oxygen ($^1O_2$), 100 µL (1 mg mL^{-1}) of the sample aqueous solution was mixed with 100 µL of 0.05 mg mL^{-1} DPBF DMSO solution, and 100 µL of the supernatant was centrifuged and the absorption spectrum was measured on a microplate reader. ROS produced by the material were detected by electron spin resonance (ESR) spectroscopy with the capture agent 2,2,6,6-tetramethylpiperidine (TEMP).[40,41]

2.7. *In vitro* antibacterial test

We investigated the antimicrobial properties of the materials by two bacteria Gram-positive *S. aureus* and Gram-negative *E. coli*. Deionized water was used to prepare materials Cur, Bi$_2$S$_3$ and Bi$_2$S$_3$/Cur at 1 mg mL^{-1}. In the antibacterial experiment, all samples were irradiated by UV for 30 min in the ultra-clean table, and then the liquid of *S. aureus* and *E. coli* was diluted to 10^7 CFU mL^{-1} through liquid medium. Add 100 µL material and 100 µL bacterial solution into the 96-well plate, and divide into two groups: dark group and light group. In the dark group, the bacteria solution in the well plate was diluted and then coated on the plate. The coated plate was incubated in a 37 °C incubator for 24 h. Finally, the antibacterial rate was calculated according to the results of the coated plate, and the calculation was as follows, A is the number of colonies:

$$\text{Antibacterial ratio}(\%) = \frac{A_{control} - A_{sample}}{A_{control}} \times 100\%. \tag{5}$$

The bacterial morphology was observed by FE-SEM. Firstly, after the completion of antibacterial activities, the *s. aureus* and *E. coli* liquid in the 96-well plate were fixed, and 2.5% glutaraldehyde was added, and fixed in the refrigerator at 4 °C for 4 h. After fixation, bacteria were washed with high-pressure steam sterilized PBS for 3 times, 15 min each time. The bacteria were then subjected to gradient dehydration with

different concentrations of ethanol (30%, 50%, 70%, 90% and 100%, 15 min per time). After drying at room temperature, the morphology of bacteria can be observed by FE-SEM.

2.8. BCA test

The BCA protein assay kit was used to detect the protein leakage of different materials to *S. aureus* and *E. coli* under light. The stock solution was first centrifuged at 6000 rpm min^{-1} for 5 min in a centrifuge at 4 °C, and the supernatant was discarded. The supernatant was washed 3 times with PBS under the same conditions and finally diluted to an OD_{600} concentration of 0.02–0.1. The diluted bacterial solution was mixed homogeneously with the material in EP tubes at 1 : 1 (200 μL + 200 μL), and then the material was treated with light under antimicrobial conditions. After centrifugation, 25 μL of the supernatant was added to 200 μL of BCA working solution and incubated in a shaker for 1 min and in a constant temperature incubator at 37 °C for 30 min. The OD_{562} value was detected and the amount of protein precipitation was determined.

2.9. ONPG test

The permeability of bacterial membrane was measured by O-nitrophenyl-β-galactoside (ONPG) method. The bacterial solution washed with PBS for 3 times and isopropyl β-D-1-thiogalactopyranoside (0.01 mg mL^{-1}) were cultured in 37 °C constant temperature incubator for 12 h, and then diluted with PBS to a working concentration of 0.05–0.1, material and bacterial solution 1 : 1 after mixing, the supernatant was taken and added into ONPG to detect OD_{420} under dark and light conditions.

2.10. Cell viability determination

Cytocompatibility tests for Cur, Bi$_2$S$_3$ and Bi$_2$S$_3$/Cur. Cytotoxicity was detected by 3-[4,5-dimethyl thiazole-2-yl]-2, 5-diphenyltetrazolium bromide (MTT, Aladin Reagent, China) method. First, NIH/3T3 mouse embryonic fibroblast cell lines were diluted to 1×10^5 cells per mL and incubated 200 μL in a 96-well plate at 37 °C in a 5% CO$_2$ incubator for 1 day. Dilute the material to 0.5 mg mL^{-1} with cell culture medium, blow evenly, discard the cell culture medium in the cell culture well plate, slowly add 200 μL of the diluted material and co-culture with the adherent cells for 1, 3 day. After that, the medium was discarded, 200 μL MTT suspension (0.5 mg mL^{-1}) was added and kept in the cell culture box for 4 h. After that, the supernatant was discarded and purple precipitate was left. After adding 200 μL DMSO, the purple precipitate was shaken on the 96-well plate for 20 min until it was dissolved. Let stand for 30 min, add 100 μL supernatant to the new 96-well plate to measure the absorption of OD_{570}.

Cell morphology and growth state were detected by cell fluorescence: the cells were fixed with diluted 4% formaldehyde solution for 10 min, and then washed with sterilized PBS for 3 times after fixation. Then, the cells were stained with fluorescein isothiocyanate (FITC) for 15 min, washed with sterilized PBS for 3 times, and then stained with 4,6-diamino-2-phenylindole (DAPI) for 30 s. After staining, the cells were washed with PBS for 3 times, and placed dry at room temperature. Finally, the cell morphology and growth state were observed and photographed under inverted fluorescence microscope (IFM, Olympus, IX73).

The hemolysis assay was performed by centrifugation of mouse blood at 4 °C (3000 rpm, 15 min) to remove the serum, and the centrifuged erythrocytes were rinsed with saline. 1 mL of 10% erythrocyte dispersion was added to H$_2$O (positive control), saline (negative control), and Cur, Bi$_2$S$_3$, Bi$_2$S$_3$/Cur (concentration 1 mg mL^{-1}, 1 ml), respectively. The supernatants were incubated at 37 °C for 4 h. The OD_{570} values were measured after centrifugation of the supernatants. The hemolysis rate of each material was calculated as eqn (6):

$$\text{Relative hemolysis rate}(\%) = \frac{C_{\text{sample}} - C_{\text{Saline}}}{C_{\text{H}_2\text{O}} - C_{\text{Saline}}} \times 100\% \quad (6)$$

C is the OD value of the supernatant.

2.11. *In vivo* animal wound healing tests

Male BALB/C mice, weighing 18–20 g, were purchased from The Animal Hospital of Huazhong Agricultural University. The animal experiment program was approved by the Animal Research Committee of Tongji Medical College, Huazhong University of Science and Technology, Wuhan. All experiments were conducted in accordance with the Regulations of the Ministry of Health of the People's Republic of China on Animal Management and the Guidelines for The Care and Use of Experimental Animals in China. Normal mice were divided into 3 groups (control, 3 M, Bi$_2$S$_3$/Cur) and 3 different time groups (2, 5, 10 days), with 12 mice in each group. After anesthesia with 16% chloral hydrate (30 mg kg^{-1}), the mouse back wound model was made with tools, and the concentration of 10^7 CFU mL^{-1} bacterial solution 10 μL and 50 μL PBS (control group, 3 M) or 50 μL Bi$_2$S$_3$/Cur (experimental group) 0.5 mg mL^{-1} were injected into the wound. The control group was wrapped with opaque sterile medical tape without any treatment. 3 M group was covered with standard 3 M wound dressing. Bi$_2$S$_3$/Cur group were irradiated with 808 nm NIR (0.67 W cm^{-2}) for 20 min and then bandaged with opaque sterile medical tape. The mice were then fed in a suitable environment. The wounds of mice were photographed on the 2nd, 5th and 10th day respectively, and the wounds were stained with Giemsa and hematoxylin and eosin (H&E). Masson staining was performed on the wound tissues of the three groups on days 2 and 10. The mouse heart, liver, spleen, lung and kidney tissues were collected 10 days after operation and stained with H&E to evaluate the toxicity of the synthetic materials.

2.12. Statistical analysis

The quantitative data of each experiment were evaluated and analyzed by one-way or two-factor ANOVA and expressed as mean standard deviation to evaluate the statistical significance

of variance. $*p < 0.05$, $**p < 0.01$ $***p < 0.001$, $****p < 0.0001$ was considered statistically significant.

3. Results and discussion

3.1. Characterization of Cur, Bi_2S_3 and Bi_2S_3/Cur

We prepared sea urchin-like Bi_2S_3/Cur hybrid material by one-pot hydrothermal method. Firstly, the evenly stirred Cur powder was added to $Bi(NO_3)_3 \cdot 5H_2O$ solution, and Cur was chelated with a small amount of Bi^{3+}, and then the evenly stirred thiourea $(CS(NH_2)_2)$ was added to the above solution for hydrothermal reaction to obtain the desired product. The size of Bi_2S_3/Cur hybrid materials was 1–4 μm (Fig. 1a). Low magnification SEM (Fig. S1a†), high magnification SEM (Fig. S1b†) and TEM (Fig. 1b) images demonstrate that Bi_2S_3/Cur has a sea urchin-like morphology consisting of a large number of bismuth sulfide rods. The high magnification SEM of Bi_2S_3/Cur (Fig. S1b†) and SEM of Bi_2S_3 (Fig. S1c and 1d†) were analyzed for comparison, and the addition of Cur sharpened the rod-like morphology on the surface of bismuth sulfide.

The TEM elemental mapping analysis corresponding to Bi_2S_3/Cur showed that Bi, S, C and O elements were uniformly distributed in the hybrid material Bi_2S_3/Cur (Fig. 1c). The HRTEM image (Fig. 1d) shows a tight interface between Cur and Bi_2S_3 with a lattice spacing of 0.360 nm corresponding to the (130) crystallographic plane of Bi_2S_3.[23] The lattice spacing of 0.642 nm is for Cur crystals. The XRD spectrum of Bi_2S_3/Cur shows the major peaks of (130), (211), (221), (002), (431) and (351) of Bi_2S_3 (Fig. 2a).[28,35] Since the hybrid material Bi_2S_3/Cur contains only a small amount of Cur, no characteristic peak of Cur was detected. The above results indicate that the phase structure of Bi_2S_3 is not changed by the addition of Cur. Fourier transform infrared spectroscopy (FTIR) analysis was performed on Bi_2S_3/Cur (Fig. 1f). The peaks displayed by Bi_2S_3/Cur were compared with those of pure Cur powder. The Cur powder shows O–H stretching vibration at 3502 cm^{-1}, corresponding to the 3452 cm^{-1} peak in Bi_2S_3/Cur with red shift. Typical Bi_2S_3/Cur peaks appear at 1627, 1602 and 1510 cm^{-1}
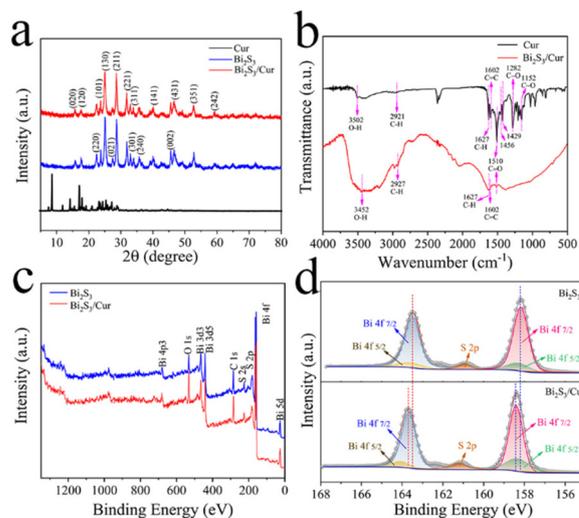
Fig. 2 (a) XRD patterns of Cur, Bi_2S_3 and Bi_2S_3/Cur. (b) FTIR spectra of Cur and Bi_2S_3/Cur. (c) XPS spectra of Bi_2S_3 and Bi_2S_3/Cur. (d) XPS spectrum of Bi 4f.

for C=C and C=O stretching vibrations, C=C in benzene ring stretching vibrations, and C=O and C=C vibrations, respectively.[36,37] This result indicates that the loading Cur on Bi_2S_3 is less.

The Cur loading in Bi_2S_3/Cur at a concentration of 0.5 mg mL^{-1} was also measured. The supernatant of the material that was continuously sonicated for 4 h was diluted 100 times and 100 μL was taken in the determination of the absorbance at 430 nm. The experiment was repeated three times, and the measured values were 0.0481, 0.0482, and 0.0498, respectively. The corresponding concentrations were calculated from Fig. S1f and 1g† as 17.451, 17.714, and 21.919 μg mL^{-1}, respectively, so the average loading was 3.8%. It was further confirmed that the Cur loading was very small.

According to the X-ray photoelectron spectroscopy (XPS) data showed the presence of Bi, S, C, O elements in Bi_2S_3/Cur, where C, O elements are stronger than the pure Bi_2S_3 signal (Fig. 2c). From the XPS spectra of Bi_2S_3/Cur, it can be seen that Bi^{3+} corresponds to Bi 4f 5/2 (164.09 eV and 158.32 eV), and Bi 4f 7/2 (163.67 eV and 158.41 eV). The fitted peaks of Bi_2S_3 correspond to the Bi 4f 5/2 orbitals (163.6 eV and 158.5 eV) and Bi 4f 7/2 orbitals (163.1 eV and 157.7 eV) (Fig. 2d). After the binding of Bi_2S_3 to Cur, the peak of Bi^{3+} shifts toward higher binding energy. In addition, the C 1s peaks C=C, C–C, C–O and C=O functional groups in Bi_2S_3/Cur correspond to 284.27 eV, 284.96 eV, 286.21 eV and 288.76 eV, respectively (Fig. S2†).[6,10]

3.2. Photocatalytic and photothermal properties

As shown in Fig. 3a, the UV-vis-NIR absorption tests were performed at 300–900 nm for the three materials at a concentration of 0.5 mg mL^{-1}, in which the OD values at 808 nm for Cur, Bi_2S_3 and Bi_2S_3/Cur were 0.123, 0.411 and 0.612, respectively. This result indicates that Bi_2S_3/Cur has better absorption
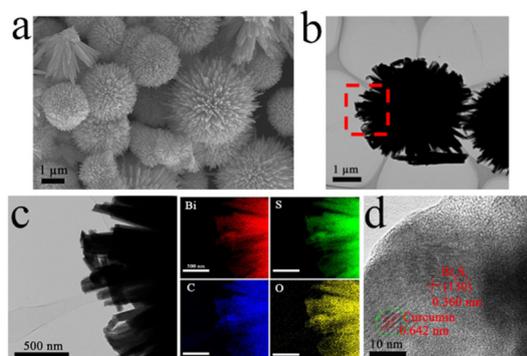

Fig. 1 Morphology and microstructure of as-synthesized materials. (a) SEM image of Bi_2S_3/Cur. Scale bar: 1 μm. (b and c) TEM and element mapping of Bi_2S_3/Cur, scale bar: 1 μm, 500 nm. (d) HRTEM, scale bar: 10 nm.
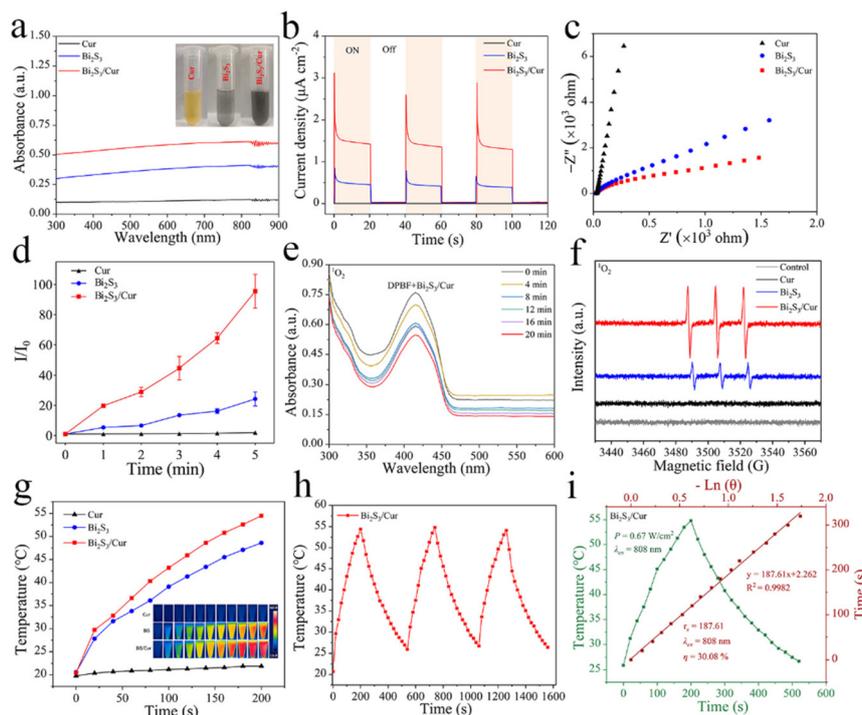
Fig. 3 Photoelectrochemical properties of Cur, Bi_2S_3, Bi_2S_3/Cur. (a) UV-visible-NIR absorption (300−900 nm) of different materials Cur, Bi_2S_3, Bi_2S_3/Cur. (b) Density of photocurrent samples and (c) EIS spectra of samples under 808 nm light irradiation. (d) ROS generation by DCFH fluorescent probe under 808 nm light irradiation. (e) $^1O_2$ was detected by DPBF degradation under 808 nm light irradiation of Bi_2S_3/Cur. (f) $^1O_2$ from ESR of Bi_2S_3/Cur (0.5 mg mL^{-1}) under 808 nm. (g) Photothermal curves of different samples irradiated by 808 nm NIR at 200 s (0.67 W cm^{-2}). (h) Photothermal cycle curve of the Bi_2S_3/Cur (3 cycles). (i) The photothermal conversion efficiency (η) of Bi_2S_3/Cur at 808 nm was calculated. Green line: calculate the heating and cooling curves of Bi_2S_3/Cur in a specific time period. Red line: calculating the cooling period time constant τ_s using linear time data.

at 808 nm than Cur and Bi_2S_3 has better light absorption ability at 808 nm. Photocurrent tests were performed on the three groups of materials. The trend of photocurrent response values at 808 nm NIR was Bi_2S_3/Cur > Bi_2S_3 > Cur. The photocurrent of Bi_2S_3/Cur was the largest and its photocatalytic effect was the best, indicating the higher separation efficiency of its photogenerated electron–hole pairs (Fig. 3b).[38] In addition, the electrochemical impedance (EIS) of the three materials was tested (Fig. 3c). The circular half warp of Bi_2S_3/Cur was minimized under 808 nm NIR light irradiation, indicating that the electrical impedance of Bi_2S_3/Cur was significantly lower and more favorable for charge transfer. The photocurrent density and EIS measurements showed that Bi_2S_3/Cur had the best photocatalytic effect, and the combination of Bi_2S_3 and Cur promoted the rapid transfer of photoelectrons.

ROS has excellent bactericidal ability, and ROS can be captured by 2,7′-dichlorofluorescein diacetate (DCFH) to measure the total ROS production of the material. The highest total ROS yield was obtained for Bi_2S_3/Cur among the three materials under 808 nm NIR irradiation (Fig. 3d). To investigate the species of ROS produced by Bi_2S_3/Cur, we used 1,3-diphenylisobenzofuran (DPBF) to detect the yield of $^1O_2$ specifically bound to DPBF. After the addition of DPBF to the control group, there was essentially no change in fluorescence intensity after 20 min of 808 nm NIR light irradiation, indicat-

ing that only very small amounts of $^1O_2$ were produced by 808 nm NIR light irradiation alone (Fig. S3a†). The decrease of DPBF fluorescence intensity in the Bi_2S_3/Cur group was more than that in the Bi_2S_3 group, indicating that more $^1O_2$ was produced in the Bi_2S_3 group, indicating that more $^1O_2$ was produced in the Bi_2S_3/Cur group (Fig. 3e and S3b†). DPBF was peaked at 415 nm and the amount of ROS production was assessed by comparing the intensity of the peaks. In addition, electron spin resonance (ESR) spectroscopy was performed to detect the ROS signal using 2,2,6,6-tetramethylpiperidine (TEMP) as the trapping agent. As shown in Fig. 3f, the signal peaks of Bi_2S_3/Cur and Bi_2S_3 were both 1:1:1, but the peak intensity of Bi_2S_3/Cur was higher than that of pure Bi_2S_3. There was no signal peak in the Cur group. DPBF and ESR results indicated that Bi_2S_3/Cur produced $^1O_2$ under 808 nm NIR irradiation. In addition, Bi_2S_3/Cur has better photothermal effect compared with Cur, Bi_2S_3. Under 808 nm NIR irradiation, the temperature of 0.5 mg mL^{-1} of Bi_2S_3/Cur increased from 20.7 °C to 54.5 °C (0.67 W cm^{-2}, 200 s). Under the same conditions, the temperature of pure Bi_2S_3 increased from 20.6 °C to 48.6 °C. and the temperature of Cur did not increase (Fig. 3g). Fig. 3h shows the photothermal cycling curves (3 cycles) of Bi_2S_3/Cur, indicating its good photothermal switching response performance and photothermal stability. By UV-vis-NIR absorption value, time constant (τ_s = 187.61)

and maximum temperature, the photothermal conversion efficiency (η) of Bi$_2$S$_3$/Cur was calculated to be 30.08% (Fig. 3i), which is higher than that of Bi$_2$S$_3$ (η = 24.45%) (Fig. S3c†). All these results indicate that Bi$_2$S$_3$/Cur has good photocatalytic and photothermal performance.

3.3. Photocatalytic mechanism

To evaluate the optical properties of Cur, Bi$_2$S$_3$ and Bi$_2$S$_3$/Cur, UV-vis-NIR diffuse reflectance spectroscopy (DRS) tests were performed on different samples. The light absorption capacity of the Bi$_2$S$_3$/Cur hybrid material at 808 nm was higher than that of Bi$_2$S$_3$ alone (Fig. 4a). According to the DRS, the band gap diagram of the material is shown in Fig. 4b. Before contact, the forbidden bandwidth of Bi$_2$S$_3$ is about 1.40 eV, which is consistent with the previously reported forbidden bandwidth of Bi$_2$S$_3$.[28] The energy band gap of Cur is about 2.19 eV. After the formation of the hybrid material, the Bi$_2$S$_3$/Cur energy band gap is 1.37 eV. In addition, work function (WF), secondary electron cutoff edge (E-cutoff) and valence band (VB) are determined by ultraviolet photoelectron spectroscopy (UPS) test (Fig. S4†). As shown in Fig. 3c, the E-cutoff of Bi$_2$S$_3$, Cur and Bi$_2$S$_3$/Cur are 16.34 eV, 16.36 eV and 16.35 eV respectively. By subtracting the excitation energy of He I (21.20 eV), the corresponding WF is 4.86 eV, 4.84 eV and 4.85 eV, respectively. The conduction band (CB) and VB of Bi$_2$S$_3$ are −0.34 eV and 1.06 eV respectively (vs. NHE, pH = 7) according to the work function and band structure. The lowest unoccupied molecular orbital (LUMO) and highest unoccupied molecular orbital (HOMO) of Cur are −1.23 eV and 0.96 eV (vs. NHE, pH = 7), respectively. Bi$_2$S$_3$/Cur band CB and valence band VB were −0.37 eV and 1.00 eV (vs. NHE, pH = 7), respect-

ively (Fig. 4d). The above results show that there is a difference in WF between Bi$_2$S$_3$ and Cur, and electronic transfer will occur on the interface after the two contact to achieve WF equilibrium. In this study, the electrons spontaneously transfer from the larger E_F Cur to the smaller E_F Bi$_2$S$_3$. A space charge area is formed at the interface where Bi$_2$S$_3$ and Cur contact (Fig. 4e). Cur loses electrons to form a positively charged layer and electrons gather on the side of Bi$_2$S$_3$ to form a negatively charged layer. The photocatalytic mechanism is that under at 808 nm NIR, the electron hole pairs of Bi$_2$S$_3$ are separated, and the photogenerated electrons transition from VB of Bi$_2$S$_3$ to CB, so the electrons concentrate on CB and the holes concentrate on VB. Due to the existence of internal electric field, part of photogenerated electrons concentrated at CB of Bi$_2$S$_3$ are transferred to Cur, which accelerates the electron transfer and reduces the recombination of electrons and holes. The CB of Bi$_2$S$_3$/Cur (−0.37 eV) is higher than that of O$_2$/O$_2^-$ (−0.33 eV),[39] indicating that oxygen can be converted to O$_2^-$ by electrons, and then ^{1}O$_2$ can be produced by electrons.

3.4. Antibacterial activity *in vitro*

The bacterial survival rate of each group was calculated using the dilution plate coating method. The results of plate coating for *S. aureus* and *E. coli* are shown in Fig. 5a and b, respectively. Compared with the control group, each experimental group showed no obvious antibacterial effect under the condition of 20 min darkness. After 808 nm NIR irradiation for 20 min, Bi$_2$S$_3$/Cur showed higher antibacterial effect than Bi$_2$S$_3$, Cur. *S. aureus* and *E. coli* were observed under FE-SEM after dark treatment and light treatment for 20 min (Fig. 5c and d). The results showed that the bacterial cell membrane
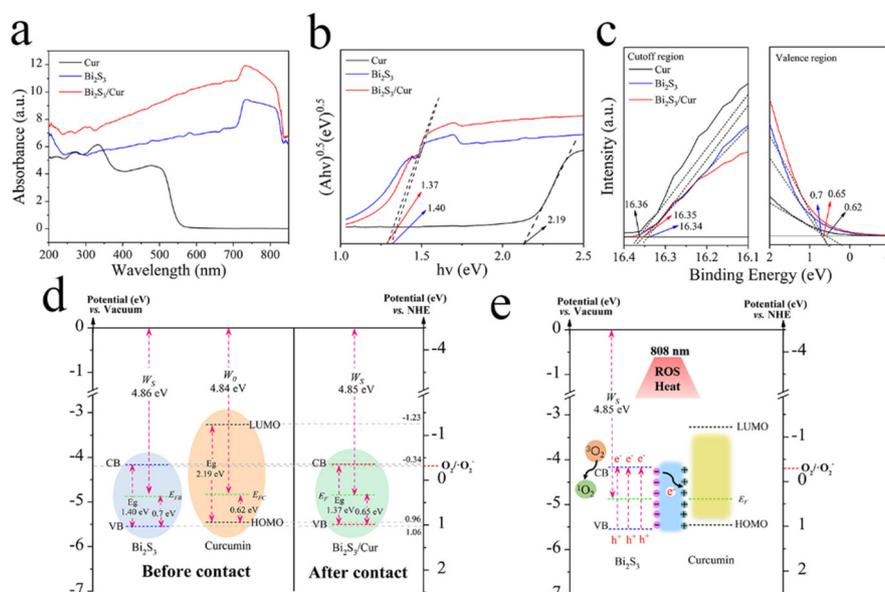

Fig. 4 Analysis of photocatalytic mechanism. (a) UV-vis-NIR diffuse reflectance spectra (DRS). (b) The corresponding Kubelka−Munk function plots derived from DRS. (c) Secondary electronic cut-off bands and valence bands for Cur, Bi$_2$S$_3$ and Bi$_2$S$_3$/Cur. (d) According to the work function and energy band structure, the energy band diagram of Bi$_2$S$_3$ and Cur before and after contact is calculated. (e) Schematic diagram of photocatalytic mechanism at 808 nm NIR.
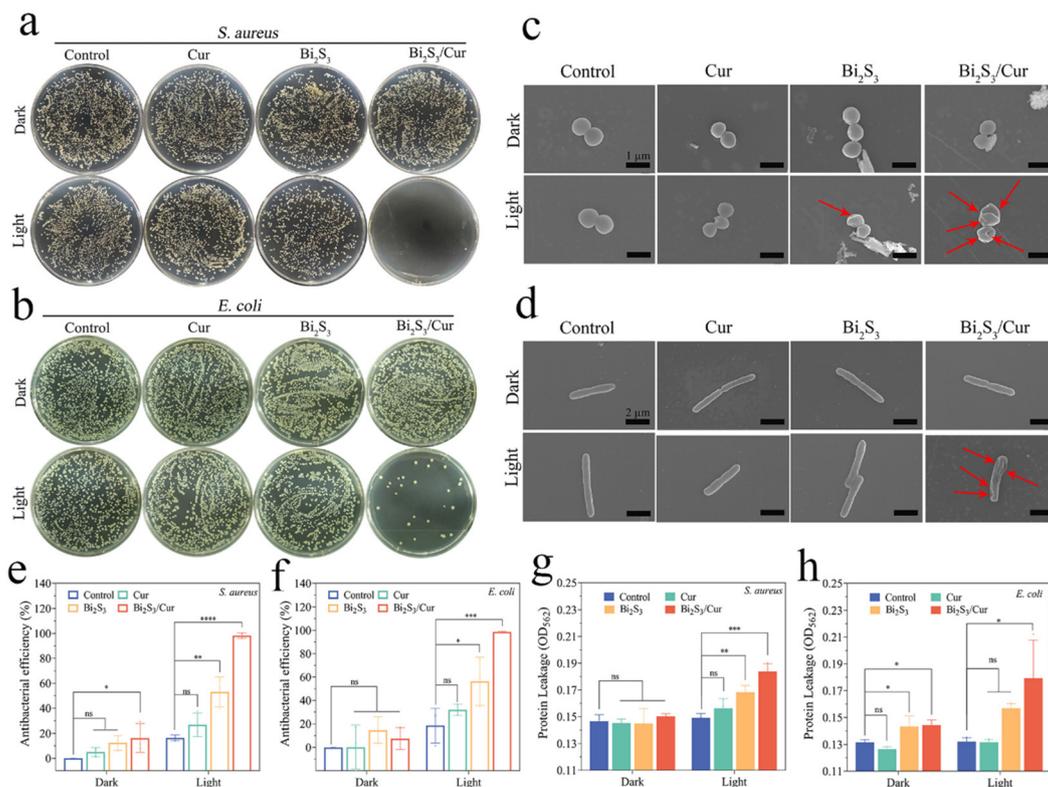
Fig. 5 Antibacterial test *in vitro*. (a and b) *S. aureus* (a) and *E. coli* (b) coated with different materials under 808 nm NIR irradiation and no irradiation for 20 min. (c) FE-SEM images of *S. aureus* morphology. Scale bars, 1 μm. (d) FE-SEM images of *E. coli* morphology. Scale bars, 2 μm. (e and f) Antibacterial effect statistics of different samples, *S. aureus* (e) and *E. coli* (f). (g and h) Protein leakage from different samples: *S. aureus* (g) and *E. coli* (h). The error bars indicate means $\pm$ SD, $n = 3$. *$p < 0.05$, **$p < 0.01$, ***$p < 0.001$, ****$p < 0.0001$.

surfaces of the dark-treated and light-treated control and Cur groups were smooth and regular, the Bi_2S_3 group had a slightly wrinkled surface, and the Bi_2S_3/Cur group had a wrinkled or ruptured surface (red arrows). In addition, the statistical plate wrap results showed that the antibacterial efficiencies of Cur, Bi_2S_3 and Bi_2S_3/Cur were 5.07%, 12.36% and 16.22% against *S. aureus*, and 0.16%, 14.73% and 7.45% against *E. coli*, respectively, under dark conditions. After 20 min of light irradiation, the antibacterial efficiencies of cur and Bi_2S_3 against *S. aureus* were 26.76% and 53.04%, respectively, and 31.96% and 56.37% against *E. coli*, respectively. Under the same conditions, the antibacterial efficiencies of Bi_2S_3/Cur against *S. aureus* and *E. coli* were 99.96% and 99.03%, respectively (Fig. 5e and f).

We further verified the damage of Bi_2S_3/Cur on *S. aureus* and *E. coli* by protein leakage experiments. There was no significant difference between Bi_2S_3/Cur under dark conditions compared to the other three groups. After illumination, there was more bacterial protein leakage in the Bi_2S_3/Cur group compared to the other groups, leading to bacterial death (Fig. 5g and h). In addition, the membrane permeability of both bacterial cell membranes was tested by ONPG hydrolysis assay, and the results showed that the membrane permeability of both bacterial groups increased after 808 nm NIR treatment for 20 min in the Bi_2S_3/Cur group. This suggests that the bac-

terial contents are more likely to leak out, leading to cell death (Fig. S5a and S5b†).

3.5. *In vitro* cytocompatibility

To assess the *in vitro* biocompatibility of the materials, we used the 3-[4,5-dimethylthiazol-2-yl]-2,5-diphenyltetrazolium bromide (MTT) method to detect the biotoxicity of the materials. The three materials at a concentration of 0.5 mg mL^{-1} were co-cultured with NIH3T3 cells under dark conditions for 1 and 3 days. Statistical analysis of the experimental results showed that the Bi_2S_3/Cur group had better biocompatibility than the Cur and Bi_2S_3 groups (Fig. 6a). The cell viability of the Bi_2S_3/Cur group was 123.54% and 127.69% on day 1 and 3, respectively, which was higher than that of the control, Cur and Bi_2S_3 groups. Different concentrations of Bi_2S_3/Cur were co-cultured with NIH3T3 cells under dark conditions for 1 and 3 days, and analysis of the experimental results showed that the promotion of cell growth was enhanced with increasing Bi_2S_3/Cur concentration (Fig. 6b). In addition, we detected the cell growth by fluorescent staining (Fig. 6c). The materials were co-cultured with NIH3T3 cells for 24 h and then NIH3T3 cells were stained. Compared with the control group, NIH3T3 cells in the Bi_2S_3/Cur group had normal morphology and normal cellular pseudopod extension, indicating that the Bi_2S_3/Cur group could promote cell proliferation and was not
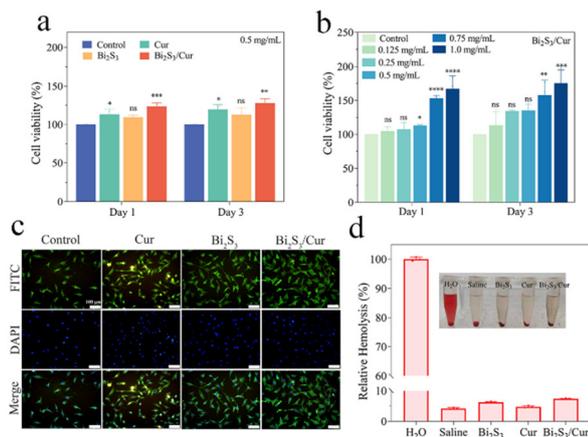
Fig. 6 Cell biocompatibility. (a) Cell viability after co-culture of Cur, Bi_2S_3 and Bi_2S_3/Cur with NIH3T3 fibroblasts for 1 and 3 days. (b) Cell viability after co-culture with NIH3T3 fibroblasts at different concentrations of Bi_2S_3/Cur for 1 and 3 days. (c) Fluorescence of cells treated with different materials. FITC staining shows cytoskeleton actin in green and DAPI staining shows nucleus in blue. Scale bars, 100 μm. (d) Hemolysis test on red blood cells of the three materials, H_2O as positive control, saline as negative control. The error bars indicate means ± SD (n = 3).

cytotoxic. As shown in Fig. 6d, the hemolysis tests of the three groups of materials were further analyzed, and the hemolysis rates of all materials were lower than 8 percent, indicating that all three groups of materials have good biocompatibility.

3.6. *In vivo* animal experiment

To verify whether material Bi_2S_3/Cur can promote wound healing of infected wounds, we constructed a mice wound model infected with *S. aureus*. As shown in Fig. S6,† the experimental design diagram of antibacterial effect of Bi_2S_3/Cur *in vivo*. As in Fig. 7a and b, we photographed and statistically analyzed the wound healing in mice at different time points. After 10 d of treatment, it was evident that the mice in the Bi_2S_3/Cur group had better wound healing than the control and 3 M groups. The wounds of the mice were measured and plotted on a line graph, and the wound healing rate in the Bi_2S_3/Cur group was 87.73%. The wound healing area of control group and 3 M group was 52.63% and 61.18%, respectively. H&E staining and Giemsa staining were performed on the traumatic sites of mice at different time points. As shown in Fig. 7c, on days 2, 5 and 10, the neutrophils in the Bi_2S_3/Cur group were significantly lower than those in the control and 3 M groups, indicating a lower inflammatory response on the traumatic surface in the material group. As shown in Fig. 7d, after Giemsa staining bacteria were stained dark blue, and it can be seen from the sections that on days 2, 5 and 10, the bacteria in the Bi_2S_3/Cur group were significantly lower than those in the control and 3 M groups, indicating a lower degree of bacterial infection on the traumatized surface of the material group.

After Masson staining, the collagen fibers in the wound tissue were stained blue, and the collagen fibers in the Bi_2S_3/Cur group were continuous and more obvious, indicating a better recovery effect in the Bi_2S_3/Cur treatment group. As

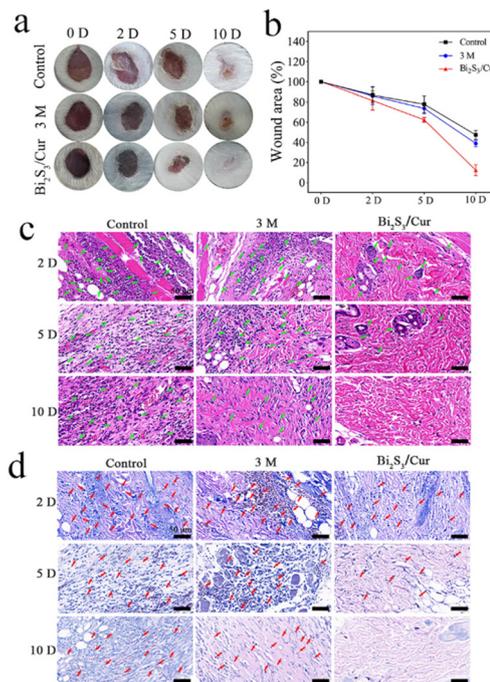**Fig. 7** Antibacterial effects of Bi_2S_3/Cur on *S. aureus* and infective wound healing *in vivo*. (a) Wound size images of the control group, 3 M dressing group and Bi_2S_3/Cur group at 0, 2, 5 and 10 days after treatment under 808 nm NIR. (b) The corresponding change in wound area was calculated according to the wound image. (c) H&E staining images showed the degree of skin tissue infection after 2, 5 and 10 days. (d) Giemsa staining images showing the degree of infection in the wound area 2, 5, 10 days after treatment. Scale bars, 50 μm.

shown in Fig. 8b, H&E staining was performed on the heart, liver, spleen, lung and kidney of mice to evaluate the *in vivo* biosafety of Bi_2S_3/Cur. The organs of the Bi_2S_3/Cur group were normal with no significant toxicological effects, indicating that the material is safe *in vivo*.
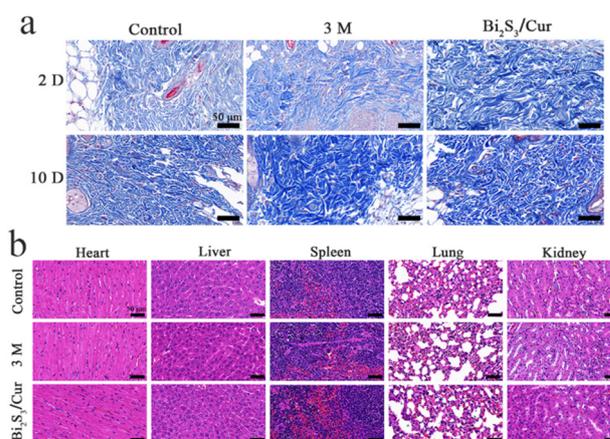

Fig. 8 Biosafety of Bi_2S_3/Cur *in vivo*. (a) Masson staining images of wound tissue on day 2 and day 10 for control, 3 M group and Bi_2S_3/Cur. (b) H&E staining images of heart, liver, spleen, lung and kidney of mice after 10 days. Scale bars, 50 μm.

4. Conclusions

We designed a rapid sterilization system of sea urchin-like Bi$_2$S$_3$/Cur hybrid material with near-infrared light response. The small molecule Cur was grown *in situ* on sea urchin-like bismuth sulfide nanorods by a one-step hydrothermal method to form the contact interface of the organic–inorganic hybrid material. Under 808 nm NIR irradiation, the electron transfer from Bi$_2$S$_3$ to Cur was accelerated, which effectively separated the photoelectron–hole pairs of bismuth sulfide, improved the photocatalytic efficiency of Bi$_2$S$_3$ and increased the generation of ROS. The results showed that Bi$_2$S$_3$/Cur could effectively kill *S. aureus* and *E. coli* using the synergistic bactericidal properties of PDT, PTT and Cur, with antibacterial rates as high as 99.96% and 99.03%, respectively. Our results indicate that this Bi$_2$S$_3$/Cur material with good biocompatibility can kill bacteria in a short time and can effectively promote the healing of bacterially infected mouse wounds, providing a new strategy for the treatment of bacterially infected wounds.

Author contributions

D. W., X. L., and S. W. developed the concept. D. W., W. S., and Y. Q. synthesized the samples and conducted the materials characterizations. D. W., X. L., D. C., and S. W. analyzed the data and co-wrote the paper. D. W., X. L., W. S., Y. Q., D. C., Y. Z., and S. W. provided important experimental insights. All the authors discussed the whole paper.

Conflicts of interest

There are no conflicts to declare.

Acknowledgements

References

1 R. A. Fisher, B. Gollan and S. Helaine, *Nat. Publ. Gr.*, 2017, **15**, 453–464.

2 J. He, Y. Qiao, H. Zhang, J. Zhao, W. Li, T. Xie, D. Zhong, Q. Wei, S. Hua, Y. Yu, K. Yao, H. A. Santos and M. Zhou, *Biomaterials*, 2020, **234**, 119763.

3 A. R. Hauser, J. Mecsas and D. T. Moir, *Clin. Infect. Dis.*, 2016, **63**, 89–95.

4 T. F. Mah, *Science*, 2021, **372**, 1153.

5 J. H. Kwon and W. G. Powderly, *Science*, 2021, **373**, 471.

6 H. Liu, J. Li, X. Liu, Z. Li, Y. Zhang, Y. Liang, Y. Zheng, S. Zhu, Z. Cui and S. Wu, *ACS Nano*, 2021, **15**, 18505–18519.

7 Z. Wang, W. Yu, N. Yu, X. Li, Y. Feng, P. Geng, M. Wen, M. Li, H. Zhang and Z. Chen, *Chem. Eng. J.*, 2020, **400**, 125877.

8 C. Wang, Y. Luo, X. Liu, Z. Cui, Y. Zheng, Y. Liang, Z. Li, S. Zhu, J. Lei, X. Feng and S. Wu, *Bioact. Mater.*, 2022, **13**, 200–211.

9 F. Chen, Y. Luo, X. Liu, Y. Zheng, Y. Han, D. Yang and S. Wu, *Adv. Healthcare Mater.*, 2022, **11**, 2200360.

10 Y. Li, X. Liu, L. Tan, Z. Cui, D. Jing, X. Yang, Y. Liang, Z. Li, S. Zhu, Y. Zheng, K. W. K. Yeung, D. Zheng, X. Wang and S. Wu, *Adv. Funct. Mater.*, 2019, **29**, 1–16.

11 G. Sheng, J. Ni, K. Xing, L. Fan, T. Dai, J. Yu, X. Dai, R. Chen, J. Wu, N. Li, J. Chen, Z. Mao and L. Li, *Colloids Interface Sci. Commun.*, 2021, **41**, 100379.

12 P. Sriram, D. S. Su, A. P. Periasamy, A. Manikandan, S. W. Wang, H. T. Chang, Y. L. Chueh and T. J. Yen, *Adv. Energy Mater.*, 2018, **8**, 1801184.

13 H. Sun, Z. Jiang, D. Wu, L. Ye, T. Wang, B. Wang, T. An and P. K. Wong, *ChemSusChem*, 2019, **12**, 890–897.

14 Q. Bai, M. Liang, W. Wu, C. Zhang, X. Li, M. Liu, D. Yang, W. W. Yu, Q. Hu, L. Wang, F. Du, N. Sui and Z. Zhu, *Adv. Funct. Mater.*, 2022, **32**, 2112683.

15 J. Chen, C. Ning, Z. Zhou, P. Yu, Y. Zhu, G. Tan and C. Mao, *Prog. Mater. Sci.*, 2019, **99**, 1–26.

16 B. Li, Y. Luo, Y. Zheng, X. Liu, L. Tan and S. Wu, *Prog. Mater. Sci.*, 2022, **130**, 100976.

17 Y. Zou, Y. Zhang, Q. Yu and H. Chen, *Biomater. Sci.*, 2021, **9**, 10–22.

18 X. Li, H. Bai, Y. Yang, J. Yoon, S. Wang and X. Zhang, *Adv. Mater.*, 2019, **31**, 1805092.

19 Y. Wang, Y. Zou, Y. Wu, T. Wei, K. Lu, L. Li, Y. Lin, Y. Wu, C. Huang, Y. Zhang, H. Chen and Q. Yu, *ACS Appl. Mater. Interfaces*, 2021, **13**, 48403–48413.

20 B. Huang, L. Tan, X. Liu, J. Li and S. Wu, *Bioact. Mater.*, 2019, **4**, 17–21.

21 Y. Luo, B. Li, X. Liu, Y. Zheng, E. Wang, Z. Li, Z. Cui, Y. Liang, S. Zhu and S. Wu, *Bioact. Mater.*, 2022, **18**, 421–432.

22 X. Yan, J. Yang, J. Wu, H. Su, G. Sun, Y. Ni and W. Sun, *Colloids Interface Sci. Commun.*, 2021, **45**, 100552.

23 L. Hong, X. Liu, L. Tan, Z. Cui, X. Yang, Y. Liang, Z. Li, S. Zhu, Y. Zheng, K. Wai, K. Yeung, D. Jing, D. Zheng, X. Wang and S. Wu, *Adv. Healthcare Mater.*, 2019, **8**, 1900835.

24 Y. Li, L. Huang, B. Li, X. Wang, Z. Zhou, J. Li and Z. Wei, *ACS Nano*, 2016, **10**, 8938–8946.

25 J. Bai, X. Chen, E. Olsson, H. Wu, S. Wang, Q. Cai and C. Feng, *J. Mater. Sci. Technol.*, 2020, **50**, 92–102.

26 P. Subramanyam, T. Vinodkumar, M. Deepa and C. Subrahmanyam, *J. Mater. Chem. C*, 2019, **7**, 6398–6405.

27 S. Wang, X. Li, Y. Chen, X. Cai, H. Yao, W. Gao, Y. Zheng, X. An, J. Shi and H. Chen, *Adv. Mater.*, 2015, **27**, 2775–2782.

28 J. Li, Z. Li, X. Liu, C. Li, Y. Zheng, K. W. K. Yeung, Z. Cui, Y. Liang, S. Zhu, W. Hu, Y. Qi, T. Zhang, X. Wang and S. Wu, *Nat. Commun.*, 2021, **12**, 1224.

29 Z. Zhou, J. Li, L. Tan, X. Liu, Y. Zheng, Z. Cui, C. Li, K. W. K. Yeung, Z. Li, Y. Liang, S. Zhu and S. Wu, *Fundam. Res.*, 2022, **2**, 496–504.

30 J. Li, Z. Zhou, X. Liu, Y. Zheng, C. Li, Z. Cui, K. W. K. Yeung, H. Zhou, J. Zou, Z. Li, S. Zhu, Y. Liang, X. Wang and S. Wu, *Matter*, 2021, **4**, 3030–3048.

31 Y. Qiao, Y. Xu, X. Liu, Y. Zheng, B. Li, Y. Han, Z. Li, K. W. K. Yeung, Y. Liang, S. Zhu, Z. Cui and S. Wu, *Nat. Commun.*, 2022, **13**, 2461.

32 L. Jin, X. Liu, Y. Zheng, Z. Li, Y. Zhang, S. Zhu, H. Jiang, Z. Cui, P. K. Chu and S. Wu, *Adv. Funct. Mater.*, 2022, **32**, 2204437.

33 S. Wanninger, V. Lorenz, A. Subhan and F. T. Edelmann, *Chem. Soc. Rev.*, 2015, **44**, 4986–5002.

34 M. Pröhl, U. S. Schubert, W. Weigand and M. Gottschaldt, *Coord. Chem. Rev.*, 2016, **307**, 32–41.

35 S. Kogularasu, B. Sriram, S. F. Wang and J. K. Sheu, *ACS Appl. Nano Mater.*, 2022, **5**, 2375–2384.

36 Y. Ma, S. Chen, W. Liao, L. Zhang, J. Liu and Y. Gao, *J. Agric. Food Chem.*, 2020, **68**, 7103–7111.

37 M. C. A. de Oliveira, F. A. G. da Silva, M. M. da Costa, N. Rakov and H. P. de Oliveira, *Adv. Fiber Mater.*, 2020, **2**, 256–264.

38 J. Li, Q. Pei, R. Wang, Y. Zhou, Z. Zhang, Q. Cao, D. Wang, W. Mi and Y. Du, *ACS Nano*, 2018, **12**, 3351–3359.

39 Y. Nosaka and A. Y. Nosaka, *Chem. Rev.*, 2017, **117**, 11302–11336.

40 F. Xu, M. Hu, C. C. Liu and S. K. Choi, *Biomater. Sci.*, 2017, **5**, 678–685.

41 M. Li, X. Liu, L. Tan, Z. Cui, X. Yang, Z. Li, Y. Zheng, K. W. K. Yeung, P. K. Chu and S. Wu, *Biomater. Sci.*, 2018, **6**, 2110–2121.